
Investigating the Adversarial Robustness of Density Estimation Using the Probability Flow ODE

Marius Arvinte Cory Cornelius Jason Martin Nageen Himayat
Intel Labs, USA

Abstract

Beyond their impressive sampling capabilities, score-based diffusion models offer a powerful analysis tool in the form of unbiased density estimation of a query sample under the training data distribution. In this work, we investigate the robustness of density estimation using the probability flow (PF) neural ordinary differential equation (ODE) model against gradient-based likelihood maximization attacks and the relation to sample complexity, where the compressed size of a sample is used as a measure of its complexity. We introduce and evaluate six gradient-based log-likelihood maximization attacks, including a novel reverse integration attack. Our experimental evaluations on CIFAR-10 show that density estimation using the PF ODE is robust against high-complexity, high-likelihood attacks, and that in some cases adversarial samples are semantically meaningful, as expected from a robust estimator.

1 Introduction

Score-based diffusion models [Song and Ermon, 2019, Ho et al., 2020, Song et al., 2020] are a powerful class of generative models that have been shown to excel at learning the score function of real-world, high-dimensional distributions of many signal modalities, such as images [Rombach et al., 2022, Saharia et al., 2022], audio [Kong et al., 2020], video [Ho et al., 2022], text [Li et al., 2022], and combinations thereof. Score-based diffusion models are also highly modular and can be used in numerous downstream applications, such as image editing [Meng et al., 2021], inverse problem solving [Chung et al., 2022], or generative classification [Chen et al., 2023].

One downstream use for a score-based model is its use as a gradient oracle in the PF ODE for unbiased density estimation [Song et al., 2020]. Density estimation is a central part of machine learning and has numerous downstream applications, such as out-of-distribution detection [Ren et al., 2019, Wang et al., 2020, Schmier et al., 2023], generative classification [Grathwohl et al., 2019, Chen et al., 2023], and uncertainty estimation [Jalal et al., 2021, Song et al., 2021b, Han et al., 2022, Luo et al., 2023]. We investigate the robustness of density estimation using the PF ODE without tying it to a specific application. Evaluating the standalone robustness of a model is highly relevant from a security perspective, where it is well-known that the robustness of the entire system depends on the weakest link [Carlini and Wagner, 2017, Carlini et al., 2019, Tramer et al., 2020], as well as from an interpretability perspective [Casper et al., 2022], where it is desired to show that robust models produce semantically meaningful samples when the attacker attempts to increase confidence of the prediction [Ilyas et al., 2019].

In this work, we investigate the outcome of end-to-end gradient-based attacks that target maximization of the PF ODE density estimate. We leverage adversarial attacks as an explainability tool [Augustin et al., 2020, Xu et al., 2020]: probing a learned density model against input-space attacks is useful for understanding what the model considers to be in-distribution. Our contributions are:

- We investigate the relation between the estimated log-likelihood using the PF ODE and sample complexity and find a negative correlation even in the adversarial setting, and that no samples with simultaneously high-likelihood and high-complexity are found, where we use the notion of *compressibility* as an empirical measure of sample complexity [Serrà et al., 2019].
- We introduce a reverse integration attack designed for the PF ODE and experimentally show that this attack successfully finds high-likelihood and semantically meaningful samples, known to be a feature of robust discriminative models [Schott et al., 2018, Ilyas et al., 2019].

2 Density Estimation using the Probability Flow ODE

Let $\mathbf{x} \in \mathbb{R}^D$ denote a high-dimensional sample, and $t \in [0, 1]$ be a scalar time index. We consider the setting in [Song et al., 2020], which characterizes the forward diffusion process by an SDE with time- and sample-dependent drift and diffusion coefficients \mathbf{f} and g , respectively:

$$d\mathbf{x} = \mathbf{f}(\mathbf{x}, t)dt + g(t)d\mathbf{w}, \quad (1)$$

where \mathbf{w} denotes a Wiener process. A central construct in our paper is the probability flow ODE [Maoutsa et al., 2020, Song et al., 2020] shown to have the same marginal densities $p_t(\mathbf{x})$ for its solution at all time indices t as the SDE in (1):

$$d\mathbf{x} = \left[\mathbf{f}(\mathbf{x}, t) - \frac{1}{2}g(t)^2\nabla_{\mathbf{x}}\log p_t(\mathbf{x}) \right] dt \stackrel{\text{def}}{=} \tilde{\mathbf{f}}(\mathbf{x}, t)dt. \quad (2)$$

We consider the sub-variance preserving formulation in [Song et al., 2020], which leads to specific choices for \mathbf{f} and g . We discuss this choice in Appendix A.1. Given a pre-trained score-based diffusion model $s_\theta(\mathbf{x}, t) \approx \nabla_{\mathbf{x}}\log p_t(\mathbf{x})$, the gradient of the flow function $\log p_t(\mathbf{x}(t))$ with respect to t is given by the neural ODE change of variable as [Chen et al., 2018]:

$$\nabla_t \log p_{\theta,t}(\mathbf{x}(t)) = -\nabla \cdot \tilde{\mathbf{f}}_\theta(\mathbf{x}, t) = -\sum_i \frac{\partial[\tilde{\mathbf{f}}_\theta(\mathbf{x}, t)]_i}{\partial x_i}, \quad (3)$$

where the notation θ subscript indicates the dependence on the score-based model. Because exactly evaluating the sum in (3) requires $\mathcal{O}(D)$ function evaluations, we use the Skilling-Hutchinson trace estimator in [Song et al., 2020] with one Monte Carlo sample using a single backward pass and a Rademacher random vector $\mathbf{z} \in [-1, 1]^D$ as:

$$\nabla \cdot \tilde{\mathbf{f}}_\theta(\mathbf{x}, t) \approx \mathbf{z}^T \nabla_{\mathbf{x}} \tilde{\mathbf{f}}_\theta(\mathbf{x}, t)\mathbf{z}. \quad (4)$$

Given a test sample \mathbf{x}_0 at time $t = 0$ serving as an initial condition for (2), off-the-shelf numerical ODE solvers can be used to solve (2) and increment the argument of the flow function up to $t = 1$, where the latent representation \mathbf{x}_1 of the sample is found. Additionally, integration of the scalar function in (3) followed by basic manipulations yields the per-sample log-likelihood estimator:

$$\log p_\theta^{\text{ODE}}(\mathbf{x}_0) = \int_0^1 \nabla \cdot \tilde{\mathbf{f}}_\theta(\mathbf{x}, t) dt + \log p_1(\text{solver}(\mathbf{x}_0)) = I_\theta^{\text{fw}}(\mathbf{x}_0) + P_\theta^{\text{fw}}(\mathbf{x}_0), \quad (5)$$

$$\log p_\theta^{\text{ODE}}(\text{solver}(\mathbf{x}_1)) = -\int_1^0 \nabla \cdot \tilde{\mathbf{f}}_\theta(\mathbf{x}, t) dt + \log p_1(\mathbf{x}_1) = I_\theta^{\text{rev}}(\mathbf{x}_1) + P_\theta^{\text{rev}}(\mathbf{x}_1). \quad (6)$$

Modern ODE solvers can be used to simultaneously obtain the value of the integral in (5) and yield \mathbf{x}_1 as the solution to (2) when the test sample \mathbf{x}_0 is the initial condition. The log-likelihood of the latent representation can be evaluated in closed-form. Both terms in the right-hand side of (5) can be viewed as functions of the input \mathbf{x}_0 , and are denoted by $I_\theta^{\text{fw}}(\mathbf{x}_0)$ and $P_\theta^{\text{fw}}(\mathbf{x}_0)$, respectively. The solver can also be used in reverse-time to recover the original sample \mathbf{x}_0 and $\log p_\theta^{\text{ODE}}(\mathbf{x}_0)$ from a latent representation, yielding $I_\theta^{\text{rev}}(\mathbf{x}_1)$ and $P_\theta^{\text{rev}}(\mathbf{x}_1)$ that solely depend on \mathbf{x}_1 as in (6).

Fast vs. accurate solvers When running end-to-end gradient-based optimization, we use a *single* and *fixed* \mathbf{z} vector shared across a relatively low number of solver iterations (e.g., 21 steps in a fixed grid Runge-Kutta 4th order solver), giving a lightweight, deterministic, and differentiable implementation. When measuring the outcome of gradient-based optimization, we *always* use a much more expensive solver routine (e.g., 1001 steps in the same solver). We denote the fast solver by $\log \tilde{p}_\theta^{\text{ODE}}$, and as the sequel shows, it is a successful approximation of the accurate solver.

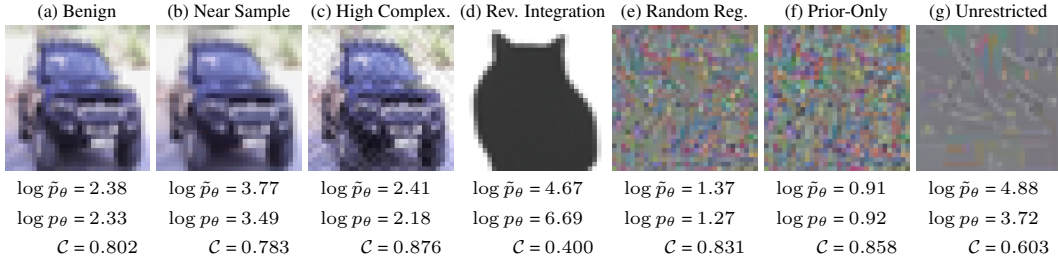


Figure 1: Sample images with fast $\log \tilde{p}_\theta$ and accurate $\log p_\theta$ estimates of $\log p_\theta^{\text{ODE}}$ and complexity \mathcal{C} . We measure (a) CIFAR-10 test image and (b)-(g) end-to-end attacks on $\log p_\theta^{\text{ODE}}$. We compute attacks (b) bounded to be near the benign sample, (c) targeting high complexity, (d) via reverse integration, (e) on random regions of input space, (f) using a prior-only objective, and (g) with no restrictions.

3 Adversarial Attacks on $\log p_\theta^{\text{ODE}}$

Our motivation is to provide an *adversarial* verification of the hypothesis that deep density estimation models tend to assign higher densities to *less complex* samples, and that high-likelihood, high-complexity samples do not exist. This has been first observed for auto-regressive and normalizing flows in [Serrà et al., 2019], but not in an adversarial setting – this does not preclude the existence of such samples. In the context of images, we use the quantitative approximation of image complexity from [Serrà et al., 2019] defined as the size of the image output when losslessly compressed using PNG defined as:

$$\mathcal{C}(\mathbf{x}) = \text{size}(\text{PNG}(\mathbf{x}))/D. \quad (7)$$

The idea behind our attacks is to find an additive perturbation δ applied to an initial sample \mathbf{x} , and constrained to lie in a set \mathcal{S} , such that it approximately solves:

$$\operatorname{argmax}_{\delta} \log p_\theta^{\text{ODE}}(\mathbf{x} + \delta) \quad \text{s.t. } \delta \in \mathcal{S}. \quad (8)$$

The outcome of the attacks applied to a set of 20 samples are shown in Figure 2, where it can be noticed that no attack was able to find samples that simultaneously have high values of $\log p_\theta^{\text{ODE}}$ and high complexity. Unless specified, we report the raw value of $\log p_\theta^{\text{ODE}}/D$ using the accurate solver.

Unrestricted attacks The adversary optimizes δ in image space, and is only restricted by the global pixel bounds. The attack uses $\mathbf{x} = \mathbf{0}$ and $\mathcal{S} = [-1, 1]^D$, and clips after every gradient step to enforce the constraint. A set of outcomes is shown in Figure 1(g). Unrestricted adversaries find monochrome images with higher likelihoods than the CIFAR-10 test set, and lower complexity. This has been previously observed for normalizing flows and auto-regressive models [Serrà et al., 2019], and shows that this bias is also present for $\log p_\theta^{\text{ODE}}$. This result also indicates that there is a strong mode of the estimated density around the all-zeroes sample, with additional results in Appendix C.

Random region attacks The adversary is restricted to optimizing δ in a random region of image space bounded by an ℓ_∞ -ball of radius ϵ . The attack uses a random, but fixed $\mathbf{x} \sim \mathcal{N}(0, 0.2)$ and $\mathcal{S} = [-\epsilon, \epsilon]^D$ with $\epsilon = 0.16$, and clips after every gradient step to enforce the constraint. We chose \mathbf{x} and ϵ such that clipping occurs infrequently. Results are shown in Figure 1(e), where it can be seen that this attack cannot find any sample with values of $\log p_\theta^{\text{ODE}}$ above the average benign test set value. The best the attacker can do is to reduce image complexity as much as possible, indicating a negative correlation between $\log p_\theta^{\text{ODE}}$ and \mathcal{C} .

Near-sample attacks This attack is similar to the random region attack. The perturbation δ is added to an in-distribution test sample. We use a random \mathbf{x} from the CIFAR-10 test set and $\mathcal{S} = [-\epsilon, \epsilon]^D$ with $\epsilon = 0.06$. Results are shown in Figure 1(b), where it can be noticed that the attacks successfully increase $\log p_\theta^{\text{ODE}}$ by reducing \mathcal{C} and making the images appeared qualitatively smoother.

High-complexity attacks The adversary uses the high frequencies in the Discrete Cosine Transform of \mathbf{x} as a differentiable approximation to \mathcal{C} , and maximizes the regularized objective $\log p_\theta^{\text{ODE}}(\mathbf{x} + \delta) + \lambda \cdot \|\text{DCT}(\mathbf{x})_{W/2:W, H/2:H}\|_2^2$, where W and H are the image dimensions. We use the same setting as the near-sample attacks, and show results in Figure 1(c) for $\lambda = 1$. We notice that our term is a

successful proxy for image complexity, and that there is always a trade-off between inducing high frequencies of the perturbation and $\log p_\theta^{\text{ODE}}$, with the attacks failing to increase $\log p_\theta^{\text{ODE}}$ for most samples.

Random region prior-only attacks This formulation uses only the prior-related term $P_\theta^{\text{fw}}(\mathbf{x})$ in the maximization objective. Figure 1(f) shows the outcome in the same setting as the random region attack. Surprisingly, we find that these attacks are as efficient as optimizing the complete expression of $\log p_\theta^{\text{ODE}}$ itself, and have more stable convergence than when $I_\theta^{\text{fw}}(\mathbf{x})$ is included. This same attack could be applied in all other settings, and Appendix B discusses its effects further.

Reverse integration attacks The attack optimizes the latent code \mathbf{x}_1 of a sample \mathbf{x}_0 using *reverse* integration of the PF ODE via the objective $\text{argmax}_\delta I_\theta^{\text{rev}}(\mathbf{x}_1 + \delta) + P_\theta^{\text{rev}}(\mathbf{x}_1 + \delta)$ and $\mathcal{S} = [-\epsilon, \epsilon]^D$. While the identities $I_\theta^{\text{fw}}(\mathbf{x}_0) = I_\theta^{\text{rev}}(\mathbf{x}_1)$ and $P_\theta^{\text{fw}}(\mathbf{x}_0) = P_\theta^{\text{rev}}(\mathbf{x}_1)$ should hold when \mathbf{x}_0 and \mathbf{x}_1 are paired in the PF ODE, they may not hold in practice. This choice may affect the gradients of these functions with respect to their inputs, ultimately affecting the convergence of a gradient-based adversary. These attacks are bounded in latent space to implicitly preserve high values of P_θ^{rev} , but unrestricted in L_∞ -norm in sample space.

Results for $\epsilon = 0.16$ are shown in Figure 1(d) in the form of samples decoded from the resulting latent codes. The resulting samples have higher likelihoods than the unrestricted attack and were found without the need of learning rate tuning. Further, the optimized samples preserve semantic meaning in some cases, e.g., the vehicle is transformed into a cat silhouette with a large value of $\log p_\theta^{\text{ODE}}$, an effect similar to the interpretability of adversarial samples designed for robust discriminative models [Ilyas et al., 2019].

4 Conclusion

Our findings have shown that the estimator $\log p_\theta^{\text{ODE}}$ is robust against high-likelihood, high-complexity attacks and is generally inversely correlated with the estimated complexity of a sample. Using this observation, a corrected density estimate formed by scaling and subtracting the complexity can be formed as per [Serrà et al., 2019], allowing $\log p_\theta^{\text{ODE}}$ to be safely used in downstream applications, such as adversarially robust out-of-distribution detection. We found that gradient-based attacks transfer from fast to accurate ODE solvers, and that certain types of well-crafted white-box attacks are successful at producing semantically meaningful samples. This is not surprising in theory, due to the adversary essentially performing gradient ascent on the *approximate* log-density of the training distribution, but is extremely relevant in practice for qualitatively measuring how well this density is learned.

4.1 Related Work

Several recent works have used forward and reverse integration of the SDE in (1) as adversarial pre-processing defenses for downstream discriminative models [Yoon et al., 2021, Nie et al., 2022, Carlini et al., 2022]. While these methods are robust against off-the-shelf attackers, other works have discussed the limitations and challenges of correctly evaluating stochastic defenses [Gao et al., 2022, Lee and Kim, 2023], as well as adversarially evaluating numerical ODE solvers [Huang et al., 2022]. The attacks we introduced deal with these challenges via a fully deterministic model and exact gradients.



Figure 2: \mathcal{C} as a function of $\log p_\theta^{\text{ODE}}$ for the benign data and the considered attacks. The top plot shows the marginal cumulative distribution function for $\log p_\theta^{\text{ODE}}$ on the benign data and each attack type.

The recent work in [Chen et al., 2023] has used the upper bound for $\log p_{\theta}^{\text{ODE}}$ derived from the SDE formulation in a robust generative classification framework, and demonstrated robustness against adaptive attacks on SDE solvers. On a different line, the recent works in [Carlini et al., 2022, Zhang et al., 2023] have derived certified robustness guarantees for discriminative models by leveraging single or multi-step sampling from the SDE.

Adversarial verification of other neural ODE models, such as flow matching [Lipman et al., 2022] or maximum likelihood trained score-based diffusion models [Song et al., 2021a] is a promising area of future research, as is formally connecting any of the training objectives with those in robust discriminative learning, such as the well-known adversarial training [Goodfellow et al., 2014, Madry et al., 2017].

Acknowledgements

This publication includes work that was funded by the Government under the Defense Advanced Research Projects Agency (DARPA) Guaranteeing AI Robustness against Deception (GARD) Program, Agreement #HR00112030001.

References

- Maximilian Augustin, Alexander Meinke, and Matthias Hein. Adversarial robustness on in-and out-distribution improves explainability. In *European Conference on Computer Vision*, pages 228–245. Springer, 2020.
- Nicholas Carlini and David Wagner. Adversarial examples are not easily detected: Bypassing ten detection methods. In *Proceedings of the 10th ACM workshop on artificial intelligence and security*, pages 3–14, 2017.
- Nicholas Carlini, Anish Athalye, Nicolas Papernot, Wieland Brendel, Jonas Rauber, Dimitris Tsipras, Ian Goodfellow, Aleksander Madry, and Alexey Kurakin. On evaluating adversarial robustness. *arXiv preprint arXiv:1902.06705*, 2019.
- Nicholas Carlini, Florian Tramer, Krishnamurthy Dj Dvijotham, Leslie Rice, Mingjie Sun, and J Zico Kolter. (certified!!) adversarial robustness for free! In *The Eleventh International Conference on Learning Representations*, 2022.
- Stephen Casper, Max Nadeau, Dylan Hadfield-Menell, and Gabriel Kreiman. Robust feature-level adversaries are interpretability tools. *Advances in Neural Information Processing Systems*, 35: 33093–33106, 2022.
- Huanran Chen, Yinpeng Dong, Zhengyi Wang, Xiao Yang, Chengqi Duan, Hang Su, and Jun Zhu. Robust classification via a single diffusion model. *arXiv preprint arXiv:2305.15241*, 2023.
- Ricky T. Q. Chen. <https://github.com/rtqichen/torchdiffeq>, 2018. URL <https://github.com/rtqichen/torchdiffeq>.
- Ricky TQ Chen, Yulia Rubanova, Jesse Bettencourt, and David K Duvenaud. Neural ordinary differential equations. *Advances in neural information processing systems*, 31, 2018.
- Hyungjin Chung, Byeongsu Sim, Dohoon Ryu, and Jong Chul Ye. Improving diffusion models for inverse problems using manifold constraints. *Advances in Neural Information Processing Systems*, 35:25683–25696, 2022.
- Yue Gao, Ilia Shumailov, Kassem Fawaz, and Nicolas Papernot. On the limitations of stochastic pre-processing defenses. *Advances in Neural Information Processing Systems*, 35:24280–24294, 2022.
- Ian J Goodfellow, Jonathon Shlens, and Christian Szegedy. Explaining and harnessing adversarial examples. *arXiv preprint arXiv:1412.6572*, 2014.
- Will Grathwohl, Kuan-Chieh Wang, Jörn-Henrik Jacobsen, David Duvenaud, Mohammad Norouzi, and Kevin Swersky. Your classifier is secretly an energy based model and you should treat it like one. *arXiv preprint arXiv:1912.03263*, 2019.

- Xizewen Han, Huangjie Zheng, and Mingyuan Zhou. Card: Classification and regression diffusion models. *Advances in Neural Information Processing Systems*, 35:18100–18115, 2022.
- Jonathan Ho, Ajay Jain, and Pieter Abbeel. Denoising diffusion probabilistic models. *Advances in neural information processing systems*, 33:6840–6851, 2020.
- Jonathan Ho, William Chan, Chitwan Saharia, Jay Whang, Ruiqi Gao, Alexey Gritsenko, Diederik P Kingma, Ben Poole, Mohammad Norouzi, David J Fleet, et al. Imagen video: High definition video generation with diffusion models. *arXiv preprint arXiv:2210.02303*, 2022.
- Yifei Huang, Yaodong Yu, Hongyang Zhang, Yi Ma, and Yuan Yao. Adversarial robustness of stabilized neural ode might be from obfuscated gradients. In *Mathematical and Scientific Machine Learning*, pages 497–515. PMLR, 2022.
- Andrew Ilyas, Shibani Santurkar, Dimitris Tsipras, Logan Engstrom, Brandon Tran, and Aleksander Madry. Adversarial examples are not bugs, they are features. *Advances in neural information processing systems*, 32, 2019.
- Ajil Jalal, Marius Arvinte, Giannis Daras, Eric Price, Alexandros G Dimakis, and Jon Tamir. Robust compressed sensing mri with deep generative priors. *Advances in Neural Information Processing Systems*, 34:14938–14954, 2021.
- Diederik P Kingma and Jimmy Ba. Adam: A method for stochastic optimization. *arXiv preprint arXiv:1412.6980*, 2014.
- Zhifeng Kong, Wei Ping, Jiaji Huang, Kexin Zhao, and Bryan Catanzaro. Diffwave: A versatile diffusion model for audio synthesis. *arXiv preprint arXiv:2009.09761*, 2020.
- Minjong Lee and Dongwoo Kim. Robust evaluation of diffusion-based adversarial purification. *arXiv preprint arXiv:2303.09051*, 2023.
- Xiang Li, John Thickstun, Ishaan Gulrajani, Percy S Liang, and Tatsunori B Hashimoto. Diffusion-lm improves controllable text generation. *Advances in Neural Information Processing Systems*, 35: 4328–4343, 2022.
- Yaron Lipman, Ricky TQ Chen, Heli Ben-Hamu, Maximilian Nickel, and Matt Le. Flow matching for generative modeling. *arXiv preprint arXiv:2210.02747*, 2022.
- Guanxiong Luo, Moritz Blumenthal, Martin Heide, and Martin Uecker. Bayesian mri reconstruction with joint uncertainty estimation using diffusion models. *Magnetic Resonance in Medicine*, 90(1): 295–311, 2023.
- Aleksander Madry, Aleksandar Makelov, Ludwig Schmidt, Dimitris Tsipras, and Adrian Vladu. Towards deep learning models resistant to adversarial attacks. *arXiv preprint arXiv:1706.06083*, 2017.
- Dimitra Maoutsa, Sebastian Reich, and Manfred Opper. Interacting particle solutions of fokker–planck equations through gradient–log–density estimation. *Entropy*, 22(8):802, 2020.
- Chenlin Meng, Yutong He, Yang Song, Jiaming Song, Jiajun Wu, Jun-Yan Zhu, and Stefano Ermon. Sdedit: Guided image synthesis and editing with stochastic differential equations. *arXiv preprint arXiv:2108.01073*, 2021.
- Weili Nie, Brandon Guo, Yujia Huang, Chaowei Xiao, Arash Vahdat, and Anima Anandkumar. Diffusion models for adversarial purification. *arXiv preprint arXiv:2205.07460*, 2022.
- Jie Ren, Peter J Liu, Emily Fertig, Jasper Snoek, Ryan Poplin, Mark Depristo, Joshua Dillon, and Balaji Lakshminarayanan. Likelihood ratios for out-of-distribution detection. *Advances in neural information processing systems*, 32, 2019.
- Robin Rombach, Andreas Blattmann, Dominik Lorenz, Patrick Esser, and Björn Ommer. High-resolution image synthesis with latent diffusion models. In *Proceedings of the IEEE/CVF conference on computer vision and pattern recognition*, pages 10684–10695, 2022.

- Chitwan Saharia, William Chan, Saurabh Saxena, Lala Li, Jay Whang, Emily L Denton, Kamyar Ghasemipour, Raphael Gontijo Lopes, Burcu Karagol Ayan, Tim Salimans, et al. Photorealistic text-to-image diffusion models with deep language understanding. *Advances in Neural Information Processing Systems*, 35:36479–36494, 2022.
- Robert Schmier, Ullrich Koethe, and Christoph-Nikolas Straehle. Positive difference distribution for image outlier detection using normalizing flows and contrastive data. *Transactions on Machine Learning Research*, 2023.
- Lukas Schott, Jonas Rauber, Matthias Bethge, and Wieland Brendel. Towards the first adversarially robust neural network model on mnist. *arXiv preprint arXiv:1805.09190*, 2018.
- Joan Serrà, David Álvarez, Vicenç Gómez, Olga Slizovskaia, José F Núñez, and Jordi Luque. Input complexity and out-of-distribution detection with likelihood-based generative models. *arXiv preprint arXiv:1909.11480*, 2019.
- Yang Song and Stefano Ermon. Generative modeling by estimating gradients of the data distribution. *Advances in neural information processing systems*, 32, 2019.
- Yang Song, Jascha Sohl-Dickstein, Diederik P Kingma, Abhishek Kumar, Stefano Ermon, and Ben Poole. Score-based generative modeling through stochastic differential equations. *arXiv preprint arXiv:2011.13456*, 2020.
- Yang Song, Conor Durkan, Iain Murray, and Stefano Ermon. Maximum likelihood training of score-based diffusion models. *Advances in Neural Information Processing Systems*, 34:1415–1428, 2021a.
- Yang Song, Liyue Shen, Lei Xing, and Stefano Ermon. Solving inverse problems in medical imaging with score-based generative models. *arXiv preprint arXiv:2111.08005*, 2021b.
- Florian Tramèr, Nicholas Carlini, Wieland Brendel, and Aleksander Madry. On adaptive attacks to adversarial example defenses. *Advances in neural information processing systems*, 33:1633–1645, 2020.
- Ziyu Wang, Bin Dai, David Wipf, and Jun Zhu. Further analysis of outlier detection with deep generative models. *Advances in Neural Information Processing Systems*, 33:8982–8992, 2020.
- Da Xu, Chuanwei Ruan, Evren Korpeoglu, Sushant Kumar, and Kannan Achan. Adversarial counterfactual learning and evaluation for recommender system. *Advances in Neural Information Processing Systems*, 33:13515–13526, 2020.
- Jongmin Yoon, Sung Ju Hwang, and Juho Lee. Adversarial purification with score-based generative models. In *International Conference on Machine Learning*, pages 12062–12072. PMLR, 2021.
- Jiawei Zhang, Zhongzhu Chen, Huan Zhang, Chaowei Xiao, and Bo Li. {DiffSmooth}: Certifiably robust learning via diffusion models and local smoothing. In *32nd USENIX Security Symposium (USENIX Security 23)*, pages 4787–4804, 2023.

Appendices

A Implementation Details

All our experiments have used a pre-trained CIFAR-10 score-based diffusion model from [Song et al., 2020], as well as building on top of their open-sourced library¹. More concretely, we used the subVP-SDE checkpoint file `checkpoint_19.pth` with the model configuration `cifar10_ddpmp_deep_continuous`. Publicly available source code for reproducing our experiments can be found at `anonymous`.

¹https://github.com/yang-song/score_sde_pytorch

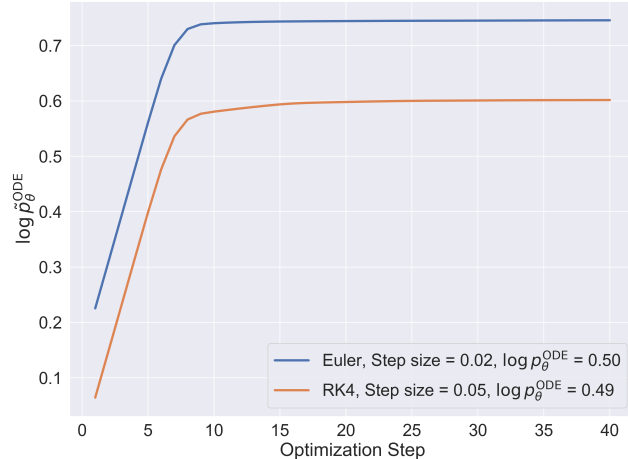


Figure 3: Convergence of gradient-based attacks using the RK4 and Euler solvers with different step sizes, but same overall complexity, respectively.

A.1 Choosing the subVP-SDE Model

Compared to its VP- and VE- counterparts, the subVP-SDE formulation for the forward diffusion process is a lesser popular choice. However, as the work in [Song et al., 2020] has shown, this is the configuration that produces the highest average test set likelihoods and is shown to perform best at estimating likelihoods even without maximum likelihood training [Song et al., 2021a].

When density estimation is desired, the VE-SDE process can be excluded because of not having a closed-form prior at $T = 1$ under which $\log p_1(\mathbf{x}_1)$ can be evaluated, and ultimately leads to lower test set likelihoods. This leaves us with a choice between the VP- and subVP-SDE formulations. To validate the claim in [Song et al., 2020], we evaluated $\log p_\theta^{\text{ODE}}$ using checkpoints from both models and found that the fast likelihood estimate is much more accurate for the subVP-SDE, hence decided to use this model in all experiments. The subVP-SDE formulation uses the functions [Song et al., 2020]:

$$\mathbf{f}(\mathbf{x}, t) = -\frac{1}{2}\beta(t)\mathbf{x}, \tag{9}$$

$$g(t) = \sqrt{\beta(t) \left(1 - e^{-2 \int_0^t \beta(s) ds}\right)}, \tag{10}$$

where $\beta(t) = (1 - t)\beta_0 + t\beta_1$ and $\beta_0 = 0.1, \beta_1 = 20$.

A.2 ODE Solver Parameters

All our experiments use a differentiable PyTorch implementation of a fourth order fixed Runge-Kutta ODE solver (RK4), using the publicly available `torchdiffeq` library [Chen, 2018].

For the fast solver that is being back-propagated throughout we used a step size of 0.05, leading to 21 unrolled steps, and an initial time of $t_0 = 0.00001$ to avoid numerical issues at $t_0 = 0$. The accurate solver for which we always report the value of $\log p_\theta^{\text{ODE}}$ for uses the same solver and starting time, but a step size of 0.001, leading to 1001 steps. Additionally, the accurate solver uses a different random \mathbf{z} at each solver step and across samples, to rule out the possibility of attacks overfitting to the fixed \mathbf{z} used with the fast solver.

We chose the RK4 solver with fewer steps as opposed to a lower order solver with more steps to trade-off some computational latency for memory, as well as to avoid potential issues caused by vanishing gradients when back-propagating through a large number of sequential function calls.

Figure 3 shows the results of end-to-end likelihood maximization through two different solvers: RK4 with step size of 0.05 and the Euler solver with step size of 0.02, having the same overall latency. The optimization targets the prior-only attack using the Adam optimizer [Kingma and Ba, 2014] with

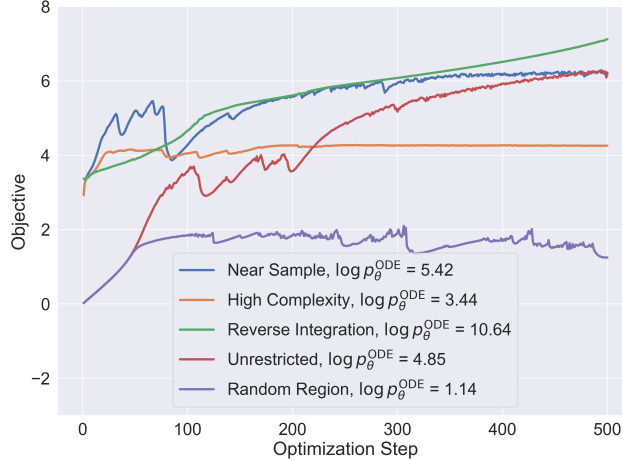


Figure 4: Convergence of gradient-based attacks on a single run. The near sample, high complexity and reverse integration attacks were all initialized using the same benign sample.

a learning rate of 0.01 and default PyTorch parameters. While both attacks converge quickly, the Euler solver over-estimates the true $\log p_{\theta}^{\text{ODE}}$ twice as much as the RK4 solver, indicating its poorer quality as an approximation when used in end-to-end gradient-based attacks.

B Attack hyper-parameters and convergence

Unless otherwise specified, all attacks are implemented using the Adam optimizer with a learning rate of 0.003, and ran for a maximum number of 500 steps. For all attacks, we have used the *exact* gradients when back-propagating through the ODE solver. Running one iteration of the fixed grid RK4 step solver with a step size of 0.05 takes approximately 34 seconds and 48 GB of memory on a single NVIDIA RTX A6000 card.

Figure 4 shows the convergence of the optimization objective for all attacks except the prior-only attack:

- The high complexity attack is generally the most stable and fastest to converge, indicative of the strict trade-off that has to be made between \mathcal{C} and $\log p_{\theta}^{\text{ODE}}$.
- The near sample is unstable in the beginning but ultimately converges after 400 steps.
- The reverse integration and unrestricted attacks stabilize but do not fully converge.
- The random region attack is the most unstable, and in some cases diverges after a number of optimization steps. This is a sign of gradient masking – intentional or not – present in random regions of space.

Overall, Figure 4 shows some of the challenges of properly tuning the considered end-to-end optimization: even with a relatively low learning rate of 0.003, some attacks are not stable, and additionally do not completely converge to their asymptotic values of $\log \tilde{p}_{\theta}^{\text{ODE}}$.

Some of these issues with the convergence of the random region attack are alleviated by the prior-only attack, for which the convergence is shown in Figure 5. In this case, convergence is drastically improved for *both* terms, and the value of $\log p_{\theta}^{\text{ODE}}$ at the end of optimization is higher, indicating that the attack is more successful. This also shows that a correlation between $I_{\theta}^{\text{rev}}(\mathbf{x}_1)$ and $P_{\theta}^{\text{rev}}(\mathbf{x}_1)$ exists, given that $I_{\theta}^{\text{rev}}(\mathbf{x}_1)$ rapidly increases in the initial steps of optimization in the prior-only attack.

C Additional Examples of Attack Outcomes

Figure 6 shows the outcome of the high-complexity attack when the value of the λ term that enforces the high-complexity of the sample is varied. This reinforces the conclusion that there is a trade-off between $\log p_{\theta}^{\text{ODE}}$ and \mathcal{C} even in the adversarial setting, and also further shows that our differentiable

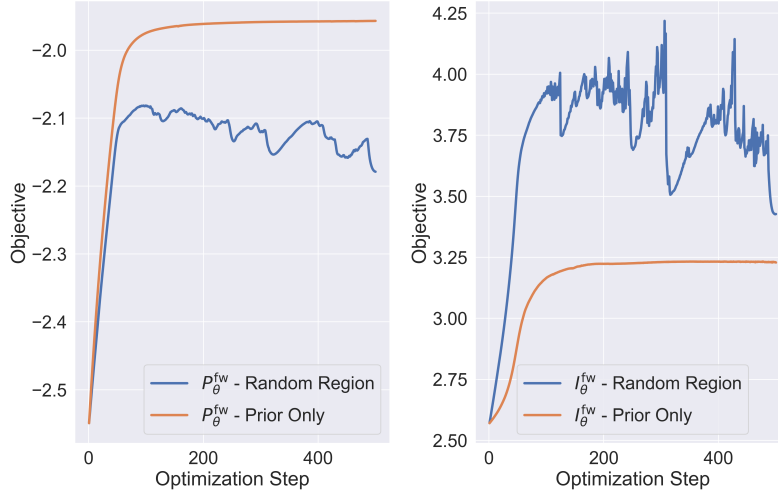


Figure 5: Impact of discarding the integral term in the random region attack, and only using the prior term in the prior-only attack. Left: The prior term across optimization. Right: The integral term across optimization.

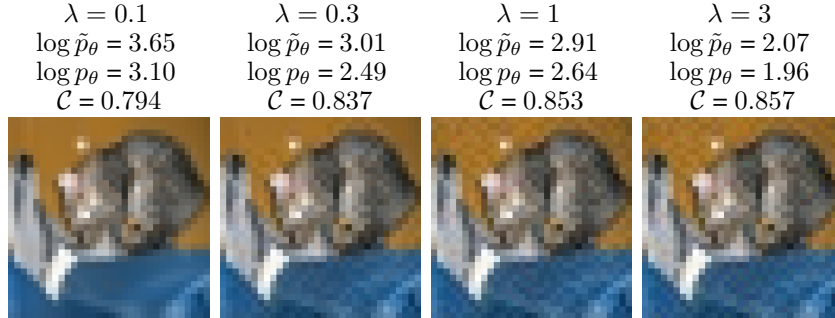


Figure 6: Outcomes of running the high-complexity attack for the same sample using different values of the hyper-parameter λ .

approximation to \mathcal{C} is accurate. Increasing λ leads to increased sample complexity, and also generally a lower estimated log-likelihood. Furthermore, in the case $\lambda = 0.3$ it can be noticed that the optimized high-frequency perturbation itself is semantic, and is mostly located around the object of interest in the sample (in this case, a cat).

Figure 8 shows eight additional outcomes in the same setting as Figure 1. In all cases, it can be qualitatively observed that:

- The near sample attack results in a smoothed version of the benign sample, hence making it more compressible and decreasing complexity.
- The reverse integration results in very smooth, monochrome patterns that, in some cases (e.g., second and third row) retain some of the semantic structure of the original sample.
- The random region (both with and without the integral term) and the unrestricted attacks result in shape structure present in the sample. This is less visible for the random region attack due to its constraints.

D Black-box Attacks

We also perform a black-box verification of the hypothesis that $\log p_\theta^{\text{ODE}}$ is biased towards estimating high values for samples that have low complexity by designing a simple set of such samples. Figure 7 shows the outcome for evaluating $\log p_\theta^{\text{ODE}}$ using the accurate solver for three types of samples:

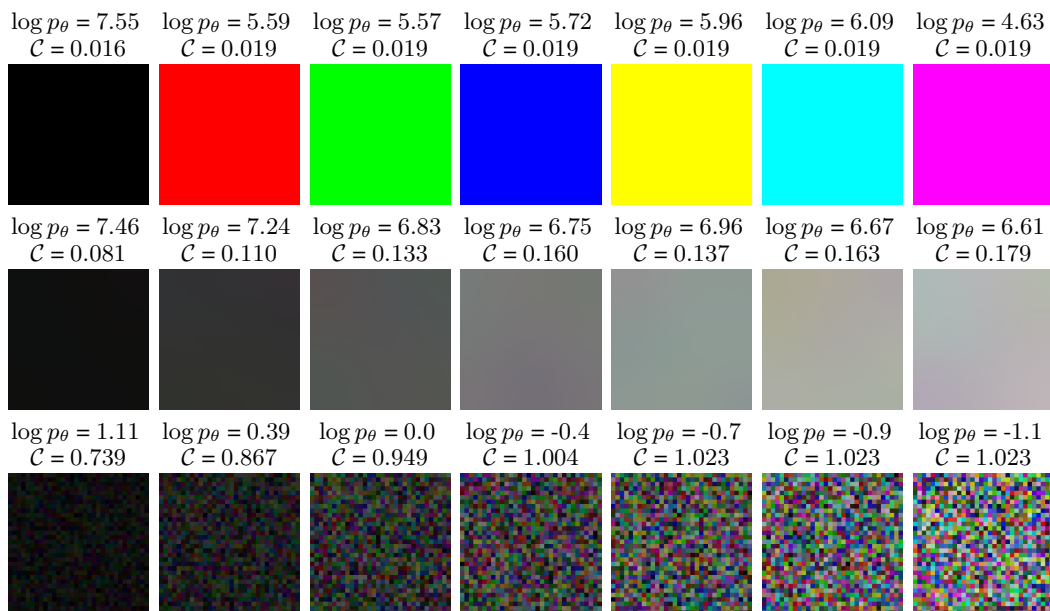


Figure 7: Outcomes of evaluating $\log p_\theta^{\text{ODE}}$ for samples with black-box (optimization free) designed high and low complexities. First row: monochrome images. Second row: Filtered uniform noise of increasing magnitude. Third row: Uniform noise of increasing magnitude.

- Monochrome samples. These samples hit the image space boundary on at least one coordinate, and as expected, have very low complexities.
- Smooth perturbations of increasing magnitude applied to the sample with all values set to -1 . We generate these perturbations by sampling uniform noise and filtering it with a two-dimensional Gaussian filter with kernel size 8.
- Random uniform noise samples of increasing standard deviation. Given that these have high complexity, we expect their estimated values of $\log p_\theta^{\text{ODE}}$ to be very low. Note that values of \mathcal{C} slightly larger than 1 can occur due to the sub-optimality of the PNG implementation.

Figure 7 shows that the expected negative correlation between $\log p_\theta^{\text{ODE}}$ and \mathcal{C} holds in this case as well: monochrome images have very high values of the estimated density, and smooth perturbations of the all-black image remain "on-manifold", as predicted by the model. Contrary, random noise images have extremely low estimated values of $\log p_\theta^{\text{ODE}}$ and can be easily detected when compared with the values of $\log p_\theta^{\text{ODE}}$ for benign, in-distribution samples.



Figure 8: Multiple examples of attack outcomes on CIFAR-10 test samples, in the same setting as Figure 1.